Topological states in α-Sn and HgTe quantum wells: A comparison of *ab initio* results

Sebastian Küfner* and Friedhelm Bechstedt

Institut für Festkörpertheorie und -optik, Friedrich-Schiller-Universität, and European Theoretical Spectroscopy Facility (ETSF), Max-Wien-Platz 1, 07743 Jena, Germany

(Received 2 October 2014; revised manuscript received 16 December 2014; published 26 January 2015)

Both α-Sn and HgTe are expected to have similar topological properties because of their inverted band structure and zero-gap character. We investigate how the different crystal symmetries and the bonding to barrier materials act to the quantum phase transition versus the thickness of the corresponding quantum well (QW) structures. They are simulated by $(SnSn)_N(CdTe)_M$ and $(HgTe)_N(CdTe)_M(110)$ superlattices. Their electronic structures and eigenstates are studied by means of first-principles calculations using the modified Becke-Johnson exchange-correlation functional and spin-orbit interaction. Significant differences are observed for the two QW materials. A topological transition between trivial insulator and quantum spin Hall phase together with the formation of topologically protected edge states are observed in the case of HgTe QWs, while these features are considerably modified for α-Sn. The different behaviors are discussed in the light of the different symmetry, spin-orbit interaction, and interface bonding. For a better understanding of the influence of the interface electrostatics also results for $(HgTe)_N(InSb)_M(110)$ systems are discussed.

DOI: 10.1103/PhysRevB.91.035311 PACS number(s): 71.70.Ej, 72.25.Mk, 73.20.At, 73.22.Gk

I. INTRODUCTION

In the last years, there was an explosion of theoretical and experimental research of topological insulators (TIs), which represent a new quantum state of matter with promising applications in spintronics and multifunctional devices [1,2]. In general, three-dimensional TIs are characterized by gapless states appearing in the fundamental gap of the projected band structure of an insulating bulk material. These metallic surface states are topologically protected due to strong spin-orbit interaction. However, there are also two-dimensional (2D) topological insulators which exhibit a quantum spin Hall (QSH) effect in a confined state [3,4]. In this respect an interesting class of materials is the zero-gap semiconductors HgTe and α-Sn with inverted band structure crystallizing in zinc blende or diamond structure. Because of the heavy elements their electronic structure is influenced by strong relativistic effects [5,6]. One is the strong spin-orbit interaction that gives rise to a huge splitting between the $p_{\frac{3}{2}}$ (Γ_{8v}) and $p_{\frac{1}{2}}$ (Γ_{7v}) derived valence bands. Together with the pronounced mass-Darwin effect the Hg $6s_{\frac{1}{2}}$ states move below the Te $5p_{\frac{3}{2}}$ states and the Sn $5s_{\frac{1}{2}}$ states tend to come in the range of the Sn $5p_{\frac{3}{2}}$ ones. As a consequence, the two zero-gap semiconductors possess an inverted band structure with the s-derived Γ_{6c} (or Γ_{7c}) band below the fourfold degenerated Γ_{8v} band which pins the Fermi level. Despite the fact that α-Sn has inversion symmetry with states with well defined parity, we apply the double-group notation of the zinc blende structure for both materials [7,8].

In 2006, Bernevig *et al.* [9] predicted HgTe quantum wells (QWs) to be two-dimensional (2D) TIs. The QWs consist of a thin HgTe layer with thickness d_1 sandwiched between layers of CdTe with relatively large fundamental gap. Due to a symmetry lowering by biaxial strain and the layered heterostructure arrangement the Γ_{8v} states split and a gap is opened in HgTe. The barrier material CdTe leads to a confinement of electrons or holes in the HgTe layers in between. Its consequence for extremely thin layers is a level inversion and a phase transition into a trivial insulator. For large thicknesses the QWs show the properties of a 2D TI together with electronic and transport properties of a quantum spin Hall (QSH) phase [1,10]. For such thicknesses d_1 HgTe films behave similarly to the bulk material with an inverted band structure. There is a critical thickness d_c where the inversion of the Γ_{8v}- and Γ_{6c}-derived bands is lifted. For $d_1 < d_c$ the HgTe QWs become trivial insulators. This picture of a 2D TI has been confirmed experimentally [11,12]. Full *ab initio* calculations of multi-QW HgTe/CdTe heterostructures with [001] and [110] orientation support this interpretation by the occurrence of topological states for $d_1 \approx d_c$ which close the gap, show edge character, are spin polarized, and are independent of the QW orientation [13].

Under small biaxial strain that opens a gap by splitting of the Γ_{8v} states the zero-gap semiconductors HgTe and α-Sn can serve also as three-dimensional (3D) TIs, which should show topologically protected metallic Dirac-cone-like states in the small gap. Recently, the topological character of thin and thick α-Sn films has been indeed demonstrated by angle-resolved photoelectron spectroscopy (ARPES) studies of slightly compressively strained α-Sn layers grown on InSb(001) substrates [14,15]. By spin-sensitive measurements the helical spin polarization of the Dirac-cone-like surface states, suggesting a protected topological character, becomes visible. However, the Dirac point is below the Fermi level in undoped samples. Strained HgTe grown epitaxially on a CdTe substrates has been identified also as a 3D TI by means of transport studies [16].

Here, we focus on 2D TIs, based on α-Sn and HgTe. In particular, we ask the question of whether or not α-Sn QWs embedded in a wide-gap semiconductor show a similar quantum phase transition versus thickness as the HgTe material. The higher space-group symmetry, the different interface properties, and the slightly changed spin-orbit interaction may modify the topological behavior. More precisely, we compare the properties of QW structures made by the different zero-gap

*sebastian.kuefner@uni-jena.de

 ©2015 American Physical Society

semiconductors α-Sn and HgTe, but both sandwiched in nearly lattice-matched CdTe barriers. The two well materials possess different space groups O_h^7 (diamond structure) and T_d^2 (zinc blende structure). The spin-orbit interaction, in particular that in the p-derived valence states, is different due to the contribution of both atoms in the unit cell (α-Sn) and mainly the anion (HgTe) to the states at the top of the valence bands, and the different local electrostatic properties due to the different bonding character in the QW layers and their interfaces with the CdTe barrier material. Therefore, we investigate the similarities and differences of the two embedded zero-gap semiconductors on the formation of quantum-well, edge, and interface states in detail. A brief description of the methodology is given in Sec. II. Results and their comparison are presented in Sec. III. Finally, in Sec. IV a summary and conclusions are given.

II. METHODS AND MODELING

For structural optimizations via the total energy we apply the density functional theory (DFT) within the local density approximation (LDA) as implemented in the Vienna *ab initio* Simulation Package (VASP) [17]. Scalar-relativistic effects and spin-orbit coupling (SOC) are taken into account. The electron-ion interaction is described by pseudopotentials that are generated within the projector-augmented wave (PAW) method [18]. The Sn $5s$, Sn $5p$, Cd $4d$, Cd $5s$, Hg $5d$, Hg $6s$, Te $5s$, and Te $5p$ electrons are treated as valence electrons. For the electronic structure studies we freeze the Sn $4d$ electrons into the core because their influence is negligibly small [19]. Moreover, with d electrons converged calculations are impossible for superlattices with large QW thicknesses. The reliability of this approximation has been demonstrated for α-Sn nanocrystals [19]. The electronic states in between the PAW spheres are expanded into a plane-wave basis set with an energy cutoff of 500 eV for bulk calculations and 275 eV in studies of the multi-QW structures. The Brillouin zone (BZ) calculations are replaced by sums over $12 \times 12 \times 12$ (bulk) or $6 \times 4 \times 1$ (multiple QWs) **k**-point meshes [20].

The Kohn-Sham eigenvalues computed by means of the LDA exchange-correlation functional underestimate fundamental gaps and interband energy distances. Moreover, in the case of zero-gap semiconductors they may give rise to a wrong ordering of the valence levels or even to a metal in the case of α-Sn [19]. A quasiparticle approach overcomes these difficulties [21]. It has recently been applied also to bulk topological insulators [22–25], among them zinc blende HgTe and other Hg chalcogenides [26,27]. However, the necessary inclusion of SOC and the need for large supercells in the modeling of the QW structures make its application impossible in the light of the computational costs. Therefore, we apply an approximate method, the Tran-Blaha method together with the modified Becke-Johnson (MBJ) semilocal exchange functional, called MBJLDA method [28]. It corrects the gap underestimations in the DFT-LDA band structures and allows for an easy inclusion of SOC (for details see, e.g., [10]). The application of the MBJLDA method is restricted to more or less homogeneous systems. Fortunately, the characteristic, material-dependent parameter CMBJ of the method can be equally chosen for α-Sn, HgTe, and CdTe to CMBJ = 1.235. This allows us to treat the band structure calculations of the corresponding multi-QW structures on the same footings.

Since CdTe is the most appropriate barrier material in terms of lattice, crystal structure, and bonding mismatch to the HgTe, as well as the large fundamental gap, we apply this zinc blende compound also as barrier material to α-Sn for a better comparison. The CdTe/AB/CdTe QW structure with an AB = SnSn or AB = HgTe in between are modeled by a corresponding multi-QW structure or superlattice with layer thicknesses $d_1 = d_{\rm AB}$ of the QWs and $d_2 = d_{\rm CdTe}$ of the barriers and consequently their sum $d_1 + d_2$ as the superlattice period. Despite the fact that usually CdTe wafers are [001] oriented, we have chosen the [110] orientation as growth direction for the multi-QW structure. The cleavage (110) faces of CdTe and HgTe are nonpolar. Together with the similar bond ionicities of both materials [29] $({\rm AB})_N({\rm CdTe})_M(110)$ superlattices used for modeling of the QW structures do not possess polar interfaces. This is in contrast to the α-Sn/CdTe(001) or (111) combinations, where the cation- and anion-terminated interfaces lead to an artificial sawtooth potential in the supercell calculations.

Because the irreducible part of the slab of diamond and zinc blende crystals in [110] direction consists of two (neutral) atomic layers with two atoms, cation and anion, in the rectangular unit cell of each atomic layer, we use basic units of two layers with four atoms and, hence, even numbers N and M. The rectangular lateral unit cell is characterized by primitive basis vectors parallel to $[\bar{1}10]$ and [001]. The numbers N and M represent the corresponding numbers of atomic layers consisting of the AB or CdTe compound [30]. In the unstrained case the layer thickness $d_1 = Na_0({\rm AB})/\sqrt{2}$ and $d_2 = Ma_0({\rm CdTe})/\sqrt{2}$ can be directly related to the lattice constants of the bulk crystals. In all explicit calculations we fix the barrier thickness to $M = 4$ and, hence, $d_2 = 1.83$ nm. Test calculations show that this barrier thickness is large enough to avoid tunneling of carriers between adjacent QWs. Assuming growth of the superlattices on CdTe substrates, we fix the in-plane lattice constants perpendicular to the superlattice axis, to $a_0({\rm CdTe})/\sqrt{2}$ along $[\bar{1}10]$ and a_0(CdTe) along [001], according to that of the barrier material. With respect to the study of edge states the choice of the [110] orientation is not a restriction, since the edge states should be topologically protected and, hence, independent of the orientation of a QW [13]. In some comparative calculations InSb is used as barrier material. For these calculations, the construction principles remain the same as in the case of CdTe barriers.

III. RESULTS AND DISCUSSION

A. Bulk band structures and band offsets

The bulk lattice constants derived within the DFT-LDA approach are $a_0 = 6.475$ Å (α-Sn), 6.450 Å (HgTe), 6.460 Å (CdTe), and 6.472 Å (InSb). These values are in agreement or slightly smaller than experimental ones [13,19]. They lead to a small tensile or compressive strain in the α-Sn and HgTe layers, respectively, which are sandwiched in CdTe barrier layers. Despite the fact that that the space-group symmetries of α-Sn and HgTe are different, we use the same denotation of energy levels for diamond and zinc blende in order to unify the

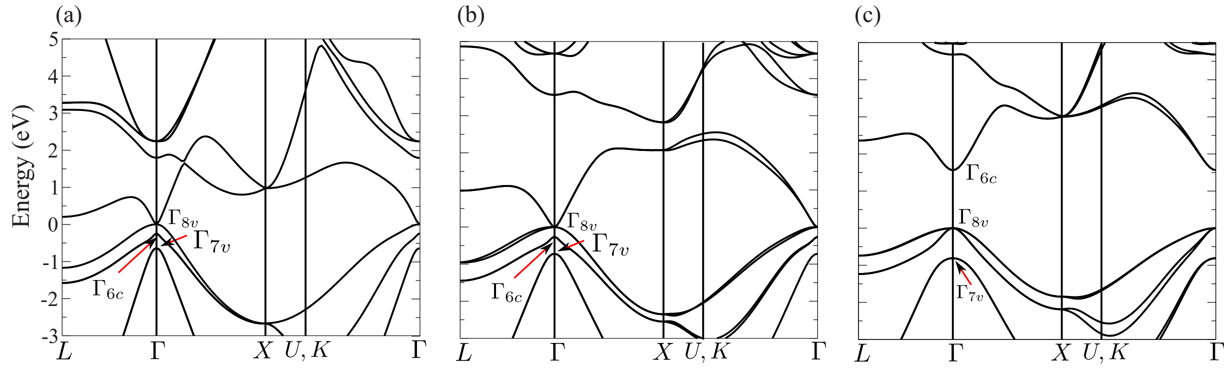

FIG. 1. (Color online) Band structures of α-Sn (a), HgTe (b), and CdTe (c) within the MBJLDA approach. The position of the Γ_{8v} level, which equals the Fermi level in the α-Sn and HgTe cases, is chosen as energy zero.

discussion. Especially, the s-derived Γ_{7c}^{+} level of α-Sn will be here denoted as Γ_{6c} as in the HgTe case [8,13]. The resulting band structures of α-Sn (diamond), HgTe (zinc blende), and CdTe (zinc blende) are depicted in Fig. 1. The band structures of the two zero-gap semiconductors are rather similar. This holds especially for the level arrangement below the Fermi level at the center Γ of the BZ. In between the spin-orbit-split bands Γ_{8v} and Γ_{7v} the s-derived $\Gamma_{6c}(\Gamma_{7c})$ level is located below the Γ_{8v} level in the case of α-Sn (HgTe). The sp-derived gap $E_g = \varepsilon(\Gamma_{6c}) - \varepsilon(\Gamma_{8v})$ is negative, $E_g = -0.23$ eV (α-Sn) and -0.26 eV (HgTe), for the two zero-gap semiconductors. These values are in reasonable agreement with measured values of $E_g = -0.29$ eV [31] ($E_g = -0.41$ eV [32]) and a result from self-consistent GW quasiparticle calculations using a band structure based on hybrid functionals as starting point, of $E_g = -0.18$ eV [33] for HgTe. On the other hand, non-self-consistent GW calculations starting from a DFT-LDA band structure performed by Sakuma *et al.* [22] give a value of $E_g = -0.6$, which is by a factor 2 larger than the experimental one. There is a suggestion that the inclusion of vertex corrections in the GW quasiparticle calculations [34] reduces the difference from the experimental value by 0.1–0.2 eV. The GW quasiparticle result based on a starting electronic structure using the HSE hybrid functional [35] of $E_g = -0.20$ eV for α-Sn [36] is also close to the MBJLDA and experimental values. The spin-orbit splittings at Γ, $\Delta_0 = \varepsilon(\Gamma_{8v}) - \varepsilon(\Gamma_{7v})$ computed within MBJLDA are 0.73 eV (HgTe) and 0.64 eV (α-Sn). For HgTe, the spin-orbit-induced valence band splitting at Γ only differs by approximately 200 meV from the measured value [31] and GW calculations [22]. The computed spin-orbit splitting in α-Sn is in excellent agreement with an experimental value of 0.8 eV [32] and close to the GW result of 0.66 eV [36].

On the contrary, the semiconductor CdTe has a positive energy gap of $E_g = 1.55$ eV within the MBJLDA. This value agrees well with experimental findings [37,38]. Therefore, one expects that CdTe forms type-III heterostructures with the two zero-gap semiconductors. There is a significant difference between the two well materials. While in the diamond-structure material α-Sn the lowest conduction band L_{6c}^{+} at the L point tends to approach the Fermi level at Γ_{8v}^{-}, the corresponding conduction band L_{6c} in HgTe is more than 1 eV above it. The reason is the difference of the atomic p-valence levels of the two atoms in a unit cell. It vanishes for equal atoms, while it approaches a large value of the order of 5.7 eV between Hg and Te [39]. In addition, the lowest conduction bands at the U,K points at the BZ boundary are separated from the Fermi level by more than 1 eV (2 eV) in the case of α-Sn (HgTe). For both materials, the highest occupied bands at U,K are more than 2 eV below the Γ_{8v} level. Consequently, these states, which are folded onto the Γ point in the surface BZ, do not influence the 2D band structure near the Fermi level. In summary, we find that the MBJLDA method reasonably describes the electronic band structures of bulk α-Sn, HgTe, and CdTe and should be, therefore, suitable for the computation of the electronic properties of their quantum well structures. In the case of layered structures made by CdTe and HgTe, the reliability of the method has been demonstrated recently [13].

Band offsets are important for the discussion of the confinement effects acting on electrons and holes in heterostructures. For their determination we use an alignment of the electrostatic potentials in the AB/CdTe superlattices and the corresponding bulk materials AB = SnSn and HgTe as well as CdTe. The procedure is described in detail elsewhere [13]. Because of the difficult interpretation due to the negative sp gaps we focus on the valence band discontinuity $\Delta E_v = \varepsilon(\Gamma_{8v},\text{AB}) - \varepsilon(\Gamma_{8v},\text{CdTe})$. Both interfaces form heterostructures where the Γ_{8v} level of HgTe (α-Sn) lies inside the fundamental gap of CdTe. In HgTe superlattices the valence band discontinuity decreases with increasing HgTe content from 0.53 eV ($N = 2$) toward 0.13 eV ($N = 12$) [13]. However, in α-Sn superlattices, the valence band discontinuity $\Delta E_v = 1.1$ eV is rather independent of the QW thickness. Moreover, the valence band discontinuity is by a factor 2 larger than the largest value calculated for HgTe QWs [13]. The different confinement situations cause significant differences in the subband structure between HgTe and α-Sn superlattices which will be discussed below.

B. Electron and hole subbands

The subband structures for three multi-QW structures are compared for α-Sn and HgTe QW films of varying thickness sandwiched between CdTe barriers in Fig. 2. There are several qualitative similarities but also quantitative discrepancies between the two different QW materials. All the superlattice systems represent insulators but with very different

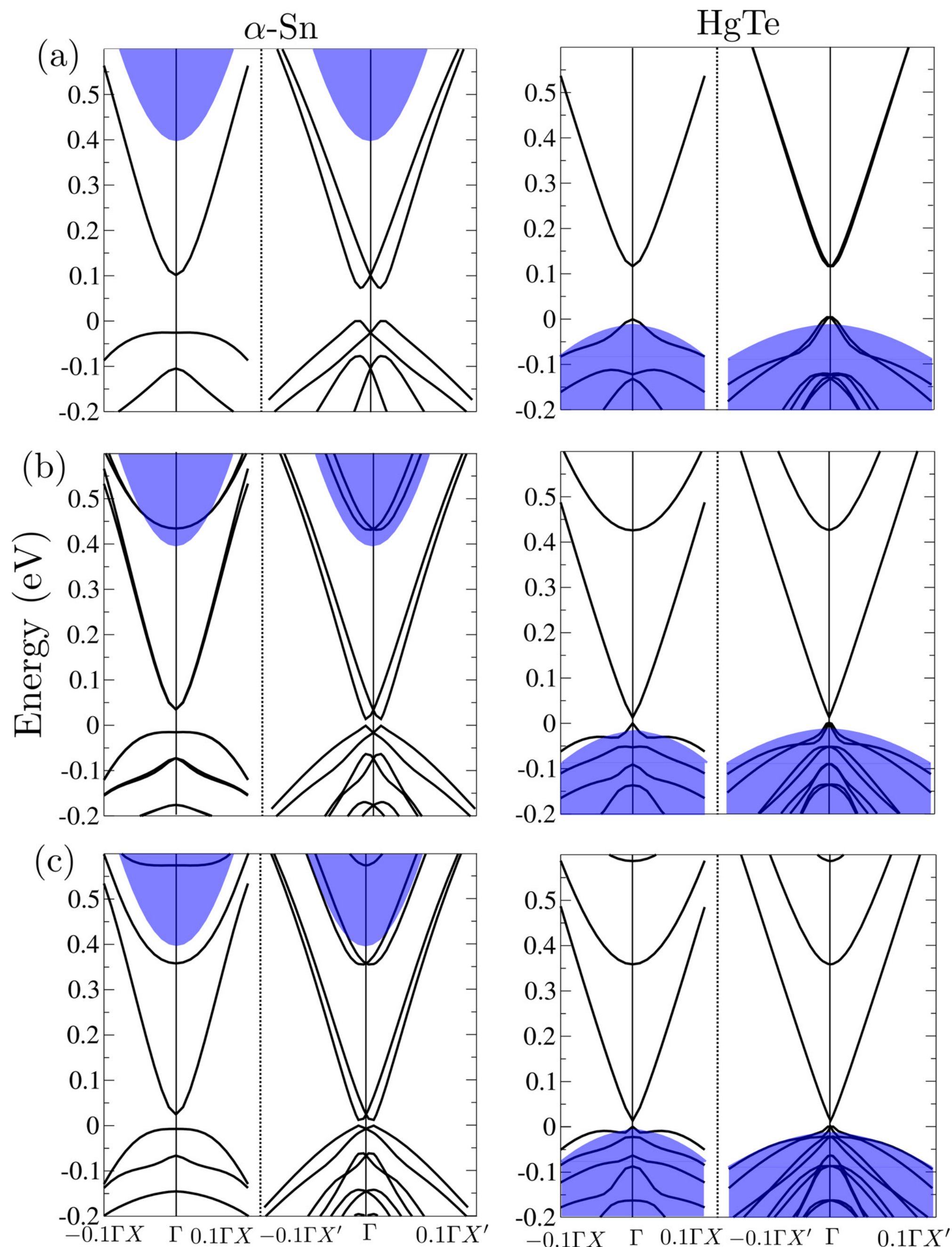

FIG. 2. (Color online) Subband structures of $(SnSn)_N(CdTe)_4(110)$ (left panels) and $(HgTe)_N(CdTe)_4(110)$ (right panels) superlattices for different QW thicknesses $N = 6$ (a), 10 (b), and 12 (c). The blue background indicates the projected bulk band structure of the CdTe barrier material. The energy of the highest occupied SL state is used as energy zero. The position of the high-symmetry points Γ, X, and X' in the respective Brillouin zone is depicted in Fig. 3(c).

fundamental energy gaps varying in the range 0.01 to 0.1 eV. The presented subbands are mainly derived from α-Sn or HgTe states. In HgTe quantum wells the contributions from CdTe to the highest occupied and the lowest unoccupied subbands is small as indicated by the energetic overlap with the projected bulk valence band structure of CdTe in Fig. 2. The same holds for α-Sn QWs despite the large valence band discontinuity.

In contrast to the ΓX direction the subbands along $\Gamma X'$, i.e., parallel to $[\bar{1}10]$, show a **k**-vector-induced splitting of all s- and p-derived subbands mainly due to spin-orbit interaction. The reason is the reduced point-group symmetry of the $(110)1 \times 1$ unit cell compared to the $(001)\sqrt{2} \times \sqrt{2}$ one [13]. Additionally, within α-Sn QWs with $N < 16$, several splittings are accompanied by a displacement of the two parabolas along $\Gamma X'$ or $-\Gamma X'$ away from the Γ point. It seems to be a clear consequence of a Rashba effect [40].

These large splittings of the subbands in $\Gamma X'$ directions and displacements of the subband extrema in α-Sn QWs are a consequence of the different electrostatic situation at the interface between CdTe and α-Sn compared to the HgTe/CdTe case. This is illustrated in Fig. 3. In the CdTe layer at the interface, one Te and one Cd atom are located at (0.5|0.5)

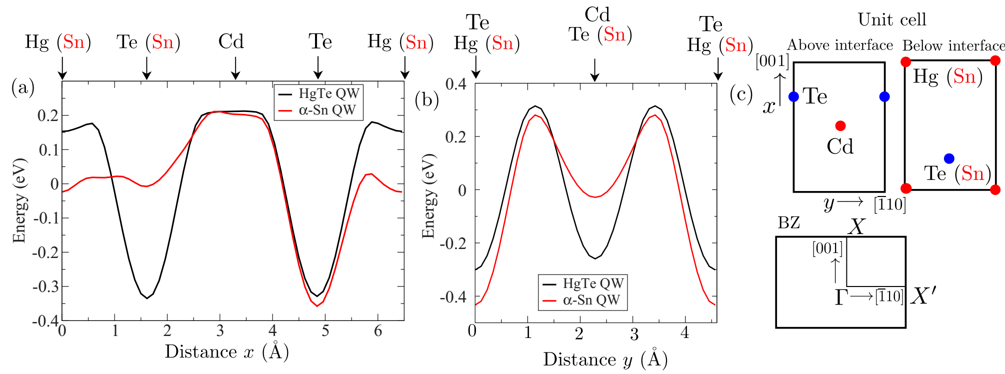

FIG. 3. (Color online) Plane-averaged local electrostatic potential for α-Sn and HgTe QWs along the x (a) and y (b) axis of the interface unit cell parallel to the interface. Only the potential of the atomic layers directly above and below the interface are taken into account. In addition, the geometry, positions of ions, high-symmetry directions, and high-symmetry points of the interface unit cell and the corresponding BZ are illustrated in (c).

(in units of the edge length) and (0.75|0), respectively, in the surface unit cell. The coordinates $(x|y)$ are illustrated in Fig. 3(c). In the case of HgTe as well material, with a HgTe layer nearest to the interface, the positions of Te (0.25|0.5) and Hg (0|0) atoms in combination with the atomic positions in the CdTe layer give rise to a mirror symmetrical electrostatic potential along the [001] (x) direction. This is clearly visible in Fig. 3(a). Along the $[\bar{1}10]$ (y) direction, two minima of the electrostatic potential caused by the Te atoms at $y = 0$ (inside the CdTe layer) and $y = 0.5$ (inside the HgTe layer) lead to a symmetric electrostatic potential as well. Consequently, in the case of HgTe(110) QWs embedded in CdTe(110) barriers, the electrostatic potential in the vicinity of the interface is symmetric in both high-symmetry directions of the surface unit cell as shown in Figs. 3(a) and 3(b). Because of the (110) interface between two II-VI compounds with similar bond ionicities no electron transfer should occur perpendicular and parallel to the interface. Therefore, no asymmetry is visible in Figs. 3(a) and 3(b). In the case of α-Sn QWs, however, the Te and Hg atoms at (0.25|0.5) and (0|0), respectively, are replaced by Sn atoms. The potential minimum caused by the Te atom inside the HgTe layer in HgTe QWs is not present. In order to fill the two resulting interface bonds Sn-Te and Sn-Cd with two electrons a transfer of half an electron is necessary between the two Sn dangling bonds of the α-Sn(110) surface pointing toward the CdTe(110) surface. In the spatial average this electron transfer gives rise to a dipole in [001] direction. Consequently, the deep potential minimum at the position of a Te atom in the HgTe surface does not anymore occur at the position of the corresponding Sn atom in the α-Sn QW case. Therefore, an asymmetric potential in [001] direction in the surface unit cell is formed as can be clearly seen in Fig. 3(a). Along the normal $[\bar{1}10]$ direction, the electrostatic potential is symmetric similarly to the HgTe case [see Fig. 3(b)]. The difference of the two minima along [001] creates an effective nonuniform electric field F_x in the [001] direction.

This resulting electric field causes the large splitting of subbands in $\Gamma X'$ direction parallel to $[\bar{1}10]$ in the α-Sn superlattices as well as the displacement of the subband extrema. Both effects can be explained with a simple Rashba spin-orbit Hamiltonian $H_{SO}^{\text{Rashba}} \propto (\mathbf{k} \times \mathbf{F}) \cdot \mathbf{s}$ with the spin operator $\mathbf{s}$ [40]. The electric field $\mathbf{F}$ has only an F_x component parallel to the [001] direction. The 2D Bloch wave vector $\mathbf{k}$ is pointed in the y direction parallel to $[\bar{1}10]$, i.e., $\Gamma X'$. Consequently, if the spin has a component parallel to the interface normal the Rashba splitting effect occurs. For the opposite direction of $\mathbf{k}$ parallel to the x axis along [001] the Rashba coupling vanishes.

The local magnetization of the two highest occupied states of a $(\text{SnSn})_6(\text{CdTe})_4$ superlattice is depicted in Fig. 4 for a $\mathbf{k}$ point near Γ along $[\bar{1}10]$. For both states the spin has a strong component parallel to the interface normal. The spin orientations of the two displaced parabola are opposite to each other, the same holds for the other pairs of displaced parabolic subbands. Together with the localization of the corresponding wave functions at the interfaces and, hence, in the region of the electric field induced by the interface potential asymmetry, the occurring Rashba splittings are explained. For increasing QWs, however, the localization behavior of the states changes

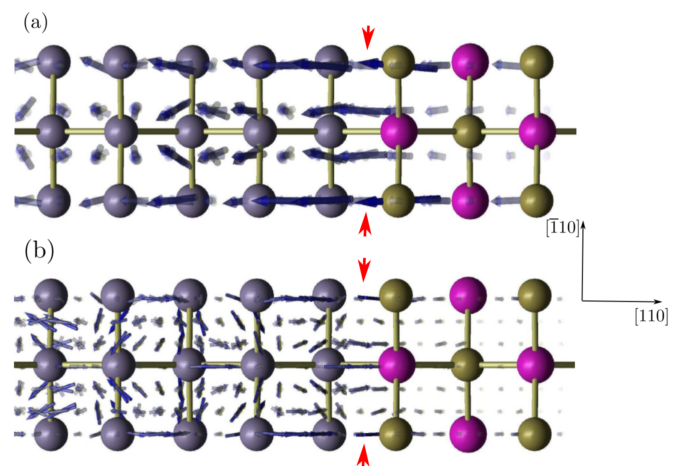

FIG. 4. (Color online) Local magnetization (blue arrows) of the highest occupied state (a) and the second highest occupied state (b) of a $(\text{SnSn})_6(\text{CdTe})_4$ QW in the vicinity of Γ in $\Gamma X'$ direction at (0.01, 0.00, 0.00) in units of the reciprocal lattice vectors in the region of the interface. Blue spheres indicate tin atoms, and Cd (Te) atoms are depicted in red (yellow). Red vertical arrows indicate the position of the interface.

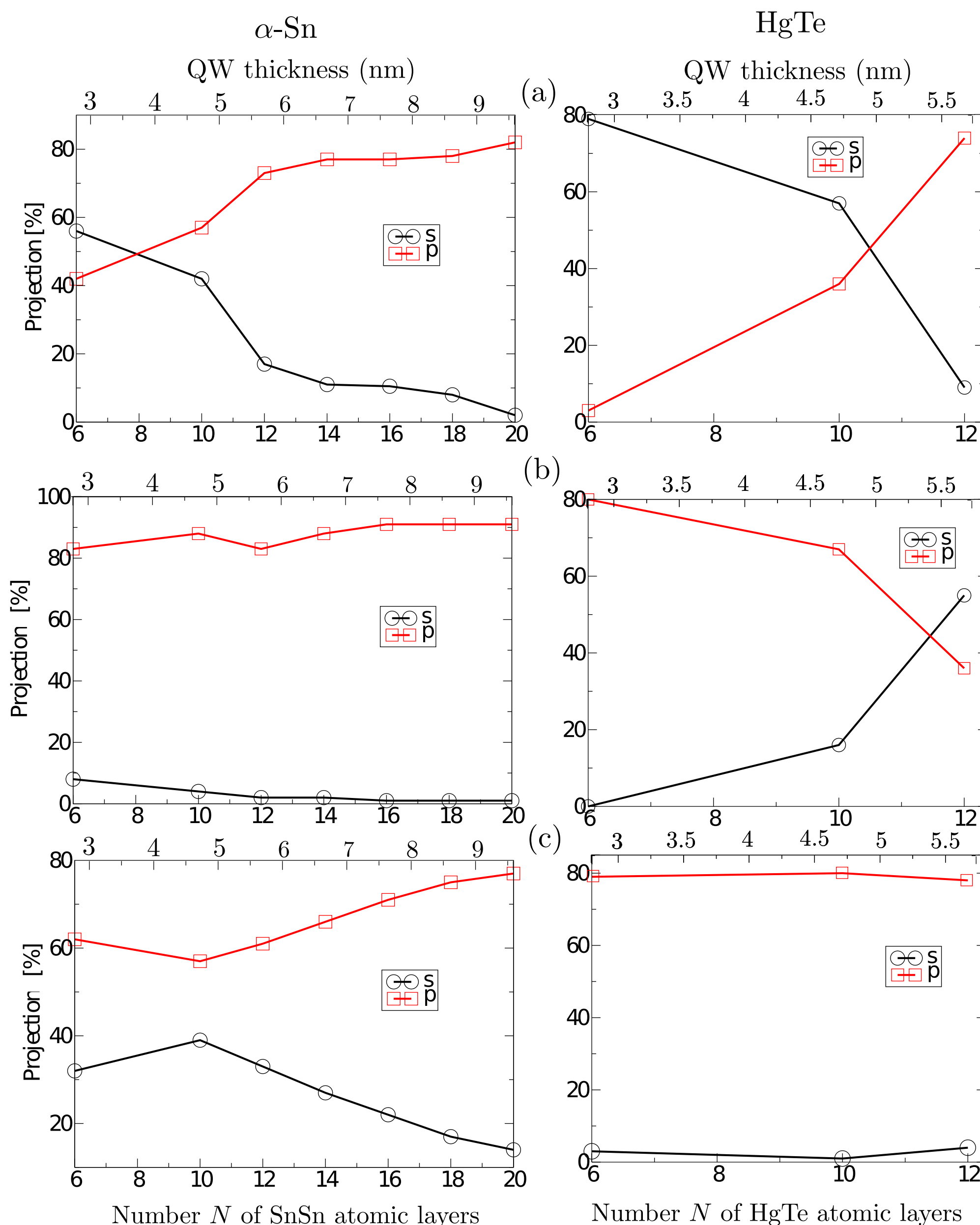

FIG. 5. (Color online) Contributions of atomic s and p orbitals on the lowest unoccupied subband (a), the highest occupied (b), and the second highest occupied subband (c) depending on the QW size. The left panels refer to α-Sn, while in the right panels the same plot for HgTe QWs is depicted.

such that a larger fraction of the wave functions is located inside the QW. Consequently, the influence of the interface potential step and, hence, the Rashba splitting decreases as clearly demonstrated in Fig. 2. For QWs larger than 14 double layers of α-Sn, no visible Rashba splitting is observed (not shown here).

Different confinements and **k**-induced spin-orbit splittings of subbands in the α-Sn QWs compared to HgTe QWs significantly influence the topological transition versus the QW thickness. This is demonstrated in Fig. 5. It shows the contributions of atomic s and p orbitals to the lowest unoccupied, the highest occupied, and the second highest unoccupied subband at Γ depending on the QW thickness. In the case of HgTe quantum wells, a topological transition from a trivial insulator to a quantum-spin Hall phase occurs at a critical thickness of 46 Å as deduced from DFT calculations [13]. Figure 5 shows that for QW thicknesses smaller than 12 double layers of HgTe, the lowest unoccupied subband at Γ is mainly formed by atomic s orbitals, while the highest occupied subband at Γ shows strong p contributions. As the s-like (p-like) subband can be identified with the Γ_6-level (Γ_8-level) character of bulk zinc blende or diamond structure crystals, the HgTe QWs with $d_1 < d_c$ show a band ordering which is similar to that of the trivial insulator CdTe. With increasing QW thickness, the energy of the s-derived subband is lowered, whereas the p-like subband is shifted toward higher energies. Consequently, at a critical thickness of $d_c = 4.6$ nm [13], there is a crossing of subbands and the level ordering is interchanged that leads to

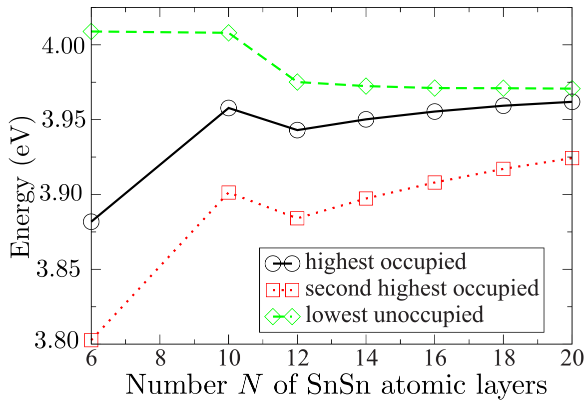

FIG. 6. (Color online) Energetic position of the highest occupied, second highest occupied, and lowest unoccupied subband at Γ depending on the QW thickness for α-Sn QWs embedded in CdTe. The average electrostatic potential is used to align the energy scales of the different $(SnSn)_N(CdTe)_4(110)$ QW structures.

an ordering $\Gamma_6 < \Gamma_8$ similar to that of HgTe bulk. In Fig. 5 this transition can be understood by the symmetry change of the lowest unoccupied subband from s- to p-like symmetry, which is accompanied by the inverse change of the highest occupied band from p to s character. This topological transition has been discussed in detail elsewhere [13].

In α-Sn QWs the situation is different. Figure 5 (left panels) indicates that the lowest unoccupied subband behaves similarly to that of HgTe QWs. For $N = 6$, the lowest unoccupied subband shows nearly 60% s contributions; the remaining 40% are due to p orbitals [see Fig. 5(a)]. With increasing thickness, the percentage of s character decreases rapidly while there is an increase in the portion of atomic p contributions. At a QW thickness of 14 (110) atomic layers of α-Sn, the ratio of p and s percentages is approximately 5:1. For even larger QWs, the atomic s orbital fraction becomes negligibly small and the band has a clear p character. The highest occupied subband, which is depicted in Fig. 5(b), is clearly p derived for all QW sizes. Finally, the second highest occupied subband [see Fig. 5(c)] shows a similar behavior as the lowest unoccupied one, but the contribution of atomic s orbitals does not decrease as rapidly as in the case of the lowest unoccupied subband. This band with pronounced s character below the Fermi level might be related to the fact that the Γ_{6c} level of α-Sn is much closer to the valence band edge than that of HgTe in the HgTe QW case due to the significantly larger valence band discontinuity in α-Sn QWs. Even for the largest QWs studied, the second highest occupied subband shows 15% s contributions. It can be summarized that despite the fact that there is an interchange in the orbital character of the lowest unoccupied subbands similar to that in HgTe QWs, the corresponding symmetry modification in the highest occupied subband is not observed. Therefore, a topological transition with an inversion of the band ordering similar to the HgTe case does not occur in α-Sn QWs with [110]-orientated interfaces. Minor contributions of atomic d orbitals are not shown in the figure. They result from bulk CdTe bands due to the large valence band discontinuity that has been discussed above.

To further investigate a possible interchange in the band ordering in the case of α-Sn QWs, the energetic positions of the three subband states closest to the Fermi level are plotted versus the QW thickness in Fig. 6. It is obvious that the fundamental energy gap decreases with increasing QW thickness from 119 meV ($N = 6$) to 9 meV ($N = 20$). This could be an indication that there might be a crossing of the highest occupied and the lowest unoccupied subband for even larger QWs. However, as discussed above and shown in Fig. 5 (left panels), for large QWs, both levels are mainly formed by atomic p orbitals. A crossing would therefore not indicate an inversion of the band ordering. The decrease of the fundamental gap which is shown in Fig. 6 is therefore more likely caused by the decreasing spatial confinement due to the increased α-Sn layer. It can be concluded that no indication for an interchange of the band ordering of Γ_{8v} and Γ_{6c} has been found in α-Sn (110) QWs embedded in CdTe barriers.

The assumption that the bonding situation with resulting local potential anisotropy and nonuniform electric field inhibits the topological transition in α-Sn can be further verified by the investigation of HgTe/InSb(110) multi-QW structures, where the barrier material CdTe is replaced by InSb, a III-V compound. The band structure of a $(HgTe)_{10}(InSb)_4(110)$ QW as depicted in Fig. 7(a) is very similar to that of a $(SnSn)_{10}(CdTe)_4(110)$ QW [left panel in Fig. 2(b)] concerning the displacement of the band extrema away from Γ and the

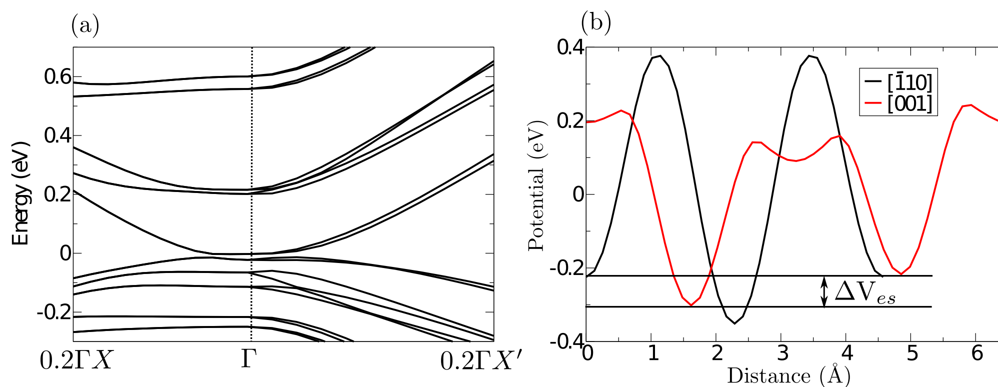

FIG. 7. (Color online) (a) Electronic band structure of a $(HgTe)_{10}(InSb)_4(110)$ QW (a) and (b) the local potential in the interface region of the same QW averaged over planes parallel to the interface normal in [001] (red line) and [$\bar{1}$10] direction (black line). The asymmetry of the electrostatic potential in [$\bar{1}$10] direction is indicated by the maximum potential difference ΔV_{es}.

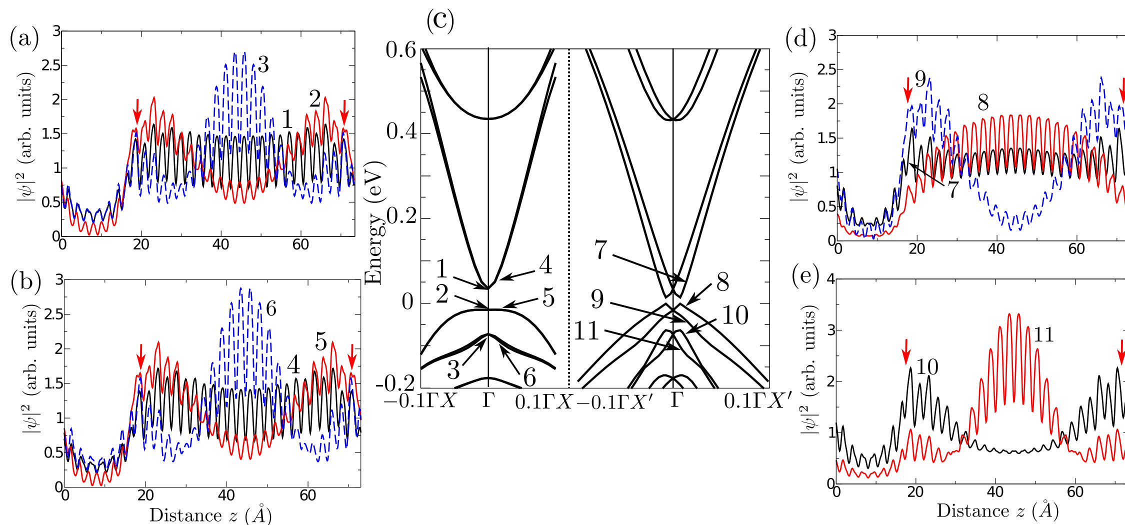

FIG. 8. (Color online) Band structure of the $N = 10$ α-Sn QW, i.e., $(SnSn)_{10}(CdTe)_4(110)$ superlattice. The panels around the band structure plot show the wave-function squares averaged over the (110) plane of the states that are marked by numbers. Different colors of the plane-averaged wave functions are chosen for reasons of a better discrimination. The respective band states are labeled by the numbers 1, 2, . . . , 10. The energy of the highest occupied states is used as energy zero. The red arrows indicate the positions of the interfaces.

large subband splittings in $\Gamma X'$ direction. Therefore, it does not show the QSH effect like the $(HgTe)_{10}(CdTe)_4$ QW of the same size [see right panel in Fig. 2(b)]. Consequently, the different bonding situation at the HgTe/InSb (II-VI compound/III-IV compound) interface compared to that of the CdTe/HgTe (II-VI compound/II-VI compound) interface must be responsible for the drastic changes in the electronic subband structure of the superlattice. This can again be understood by an electron transfer between the Hg-Sb and Te-In interface bonds of about 0.25 electrons along [001]. The resulting asymmetry of the electrostatic potential in [001] direction in the interface region, which is shown in Fig. 7(b), is similar to the situation at the α-Sn/CdTe interface. With regard to the interface electrostatics, the In and Sb atoms in the first atomic layer behave qualitatively similar to the two Sn atoms in the first atomic layer in the well film. Consequently, the electronic structure of InSb/HgTe QWs shows a behavior analogous to α-Sn/CdTe superlattices. There is only a quantitative difference due to the different net electron transfers along [001].

C. Edge states

For the HgTe QWs with weak **k**-induced SOC splittings of the subbands along the $\Gamma X'$ line the properties of the states at Γ for the lowest empty subband and highest occupied subband have been recently studied [13]. For QW thicknesses $d_1 \approx d_c$ near the critical one d_c, where the band inversion happens, their edge state character has been demonstrated by their spin polarization, their chirality, their independence of the interface orientation, and their localization near the interfaces in the QW material. In addition, the almost linear band dispersion has been proven together with the appearance of Dirac cones. Of course, the extremely small gap at Γ leads to a slight smoothening of the apex regions of the cones. For that reason we focus the study on the state properties of the lowest empty and highest occupied subbands in the case of α-Sn QWs in Fig. 2. For one example $(SnSn)_{10}(CdTe)_4(110)$ we study the wave functions at Γ but also at the shifted position (0,0.01) (in units of the reciprocal lattice) in the surface BZ, at which the extrema of the subbands occur and in [100] direction at (0.01,0) in which the subband splitting is negligibly small. The wave-function squares in Fig. 8(a) show the characteristic atomic oscillations. Most interesting are however the envelopes of these functions because they directly describe their localization behavior.

At Γ, the lowest empty subband and the highest occupied one are localized in the QW material. They clearly indicate maxima of the probability density close to the interfaces with a relatively slow decay into the QW material. Therefore, both states show an important property of edge states, their localization near the interfaces. The second highest occupied band is localized in the center of the α-Sn material and can be identified with a lowest $n = 1$ confined state as occurs in a rectangular potential well. The localization of the envelope functions of these three subband states closest to the Fermi level does not change at the **k**-point (0.01,0) in the vicinity of Γ in [001] direction where the twofold degeneracy of the subbands is not lifted [see Fig. 8(b)].

The situation does completely change in the $[\bar{1}10]$ direction of the interface BZ where the large subband splittings due to the local electric field in the interface plane via the Rashba effect occur as depicted in Figs. 8(d) and 8(e). The envelope functions [Figs. 8(d) and 8(e)] show that the lowest unoccupied band still exhibits a slightly elevated probability density at the interface while the decay inside the α-Sn layer is very small. Most interesting is the behavior of the four highest occupied bands. In the $\Gamma X'$ direction, each pair splits into an upper state that is localized at the interfaces and decays inside the α-Sn layer, and a lower one that is similar to a $n = 1$ confined state due to Rashba splitting as explained in the previous section.

The QSH phase that occurs in HgTe QWs is not present in the case of α-Sn QWs, because the subband states, that are localized at the interface, do not possess the characteristic spin polarization perpendicular to the interface normal. In fact, as

shown in Fig. 4, the subband states possess a spin orientation parallel to the interface normal which leads to the Rashba splitting of states in [$\bar{1}$10] direction as discussed above. In the opposite direction [001] without subband splitting, Kramers degeneracy of these states occurs. The interface states are therefore no longer chiral edge states that could lead to spin currents.

IV. SUMMARY AND CONCLUSIONS

We have applied the modified Becke-Johnson exchange-correlation functional including spin-orbit interaction to study the size-dependent electronic properties of embedded α-Sn quantum wells, especially a possible quantum phase transition along the thickness and the carrier confinement as well as the occurrence of edge states. For the purpose of comparison with HgTe, another zero-gap semiconductor with inverted bulk band structure, we have investigated CdTe as barrier material with real (110) interfaces to the α-Sn material in the quantum wells. Furthermore, test calculations of HgTe QWs with InSb as barrier material were performed.

Compared to HgTe, in the α-Sn case the interpretation of the electronic structure and, therefore, of the topological states is much more complicated. The main reason is the occurrence of an asymmetric electrostatic potential at the α-Sn/CdTe(110) interface in the [001] direction. The accompanying electric field leads to an additional symmetry break, which significantly influences the edge states. The most striking effect is, however, the **k**-induced splitting and, for many subbands, the displacement of band extrema out of Γ together with a spin polarization parallel to the interface normal for **k** vectors parallel to [$\bar{1}$10]. These phenomena can be interpreted as consequences of a Rashba effect due to an asymmetric electrostatic potential in the interface region. This has been further verified by the calculations of the electronic structure of HgTe/InSb(110) QWs that shows similar electrostatic interface properties to those of α-Sn/CdTe(110) QWs and consequently possess very similar electronic subband structures.

Similar tendencies for the orbital character of the lowest unoccupied subbands in α-Sn QWs have been found as observed for HgTe QWs. With increasing well thickness we found a transition in the orbital character of the lowest unoccupied subband from s-like to p-dominated character for both materials. For small well thicknesses the multi-QW systems behave therefore as trivial insulators with a normal energetic ordering of s and p states near the Γ point. However, there are significant differences in the orbital character of the highest occupied subbands between both well materials. In HgTe QWs, a transition of the highest occupied subband from p- to s-like is found which leads to an interchange in the band ordering. This is not the case for α-Sn QWs, where the orbital character of these bands remains p-like for all studied QW thicknesses. Moreover, despite the occurrence of interface states, they do not possess the characteristic spin polarization of chiral edge states and α-Sn QWs therefore cannot be interpreted a realization of the QSH phase in contrast to HgTe/CdTe QWs. As the main reason for the different behavior of α-Sn and HgTe(110) QWs embedded in CdTe, the different interface bonding and accompanying interface electrostatics has been identified.

ACKNOWLEDGMENTS

We acknowledge financial support by the Austrian Science Fund (FWF) through Special Research Programme F25 “Infrared optical nanostructures” (SFB IR-ON).

[1] M. Z. Hasan and C. L. Kane, Rev. Mod. Phys. **82**, 3045 (2010).
[2] J. Moore, Nature (London) **464**, 194 (2010).
[3] C. L. Kane and E. J. Mele, Phys. Rev. Lett. **95**, 146802 (2005).
[4] C. L. Kane and E. J. Mele, Phys. Rev. Lett. **95**, 226801 (2005).
[5] I. Tsidilkowski, *Gapless Semiconductors—a New Class of Materials* (Akademie-Verlag, Berlin, 1988).
[6] *Springer Handbook of Condensed Matter and Materials Data* (Springer Verlag, Berlin, 2005).
[7] R. Enderlein and N. J. M. Horing, *Fundamentals of Semiconductor Physics and Devices* (World Scientific Publishing, New York, 1997).
[8] P. Yu and M. Cardona, *Fundamentals of Semiconductors* (Springer, Berlin, 1996).
[9] B. Andrei Bernevig, T. L. Hughes, and S.-C. Zhang, Science **314**, 1757 (2006).
[10] X.-L. Qi and S.-C. Zhang, Rev. Mod. Phys. **83**, 1057 (2011).
[11] M. König, S. Wiedmann, C. Brüne, A. Roth, H. Buhmann, L. Molenkamp, X.-L. Qi, and S.-C. Zhang, Science **318**, 766 (2007).
[12] A. Roth, C. Brüne, H. Buhmann, L. W. Molenkamp, J. Maciejko, X.-L. Qi, and S.-C. Zhang, Science **325**, 294 (2009).
[13] S. Küfner and F. Bechstedt, Phys. Rev. B **89**, 195312 (2014).
[14] A. Barfuss, L. Dudy, M. R. Scholz, H. Roth, P. Höpfner, C. Blumenstein, G. Landolt, J. H. Dil, N. C. Plumb, M. Radovic, A. Bostwick, E. Rotenberg, A. Fleszar, G. Bihlmayer, D. Wortmann, G. Li, W. Hanke, R. Claessen, and J. Schäfer, Phys. Rev. Lett. **111**, 157205 (2013).
[15] Y. Ohtsubo, P. Le Fèvre, F. Bertran, and A. Taleb-Ibrahimi, Phys. Rev. Lett. **111**, 216401 (2013).
[16] C. Brüne, C. X. Liu, E. G. Novik, E. M. Hankiewicz, H. Buhmann, Y. L. Chen, X. L. Qi, Z. X. Shen, S. C. Zhang, and L. W. Molenkamp, Phys. Rev. Lett. **106**, 126803 (2011).
[17] G. Kresse and J. Furthmüller, Phys. Rev. B **54**, 11169 (1996).
[18] G. Kresse and D. Joubert, Phys. Rev. B **59**, 1758 (1999).
[19] S. Küfner, J. Furthmüller, L. Matthes, M. Fitzner, and F. Bechstedt, Phys. Rev. B **87**, 235307 (2013).
[20] H. J. Monkhorst and J. D. Pack, Phys. Rev. B **13**, 5188 (1976).
[21] W. G. Aulbur, L. Jönsson, and J. W. Wilkins, in *Advances in Research and Applications*, Solid State Physics, Vol. 54, edited by H. Ehrenreich and F. Spaepen (Academic Press, Singapore, 1999), pp. 1–218.
[22] R. Sakuma, C. Friedrich, T. Miyake, S. Blügel, and F. Aryasetiawan, Phys. Rev. B **84**, 085144 (2011).
[23] O. V. Yazyev, E. Kioupakis, J. E. Moore, and S. G. Louie, Phys. Rev. B **85**, 161101(R) (2012).

[24] I. A. Nechaev and E. V. Chulkov, Phys. Rev. B **88**, 165135 (2013).
[25] C.-H. Park and S. G. Louie, Phys. Rev. Lett. **109**, 097601 (2012).
[26] I. Aguilera, C. Friedrich, G. Bihlmayer, and S. Blügel, Phys. Rev. B **88**, 045206 (2013).
[27] T. Hirahara, G. Bihlmayer, Y. Sakamoto, M. Yamada, H. Miyazaki, S.-i. Kimura, S. Blügel, and S. Hasegawa, Phys. Rev. Lett. **107**, 166801 (2011).
[28] F. Tran and P. Blaha, Phys. Rev. Lett. **102**, 226401 (2009).
[29] W. Harrison, *Electronic Structure and the Properties of Solids* (Dover, New York, 1989).
[30] F. Bechstedt, *Principles of Surface Physics* (Springer-Verlag, Berlin, 2003).
[31] N. Orlowski, J. Augustin, Z. Gołacki, C. Janowitz, and R. Manzke, Phys. Rev. B **61**, R5058 (2000).
[32] S. Groves, C. Pidgeon, A. Ewald, and R. Wagner, J. Phys. Chem. Solids **31**, 2031 (1970).
[33] A. Svane, N. E. Christensen, M. Cardona, A. N. Chantis, M. van Schilfgaarde, and T. Kotani, Phys. Rev. B **84**, 205205 (2011).
[34] A. Fleszar and W. Hanke, Phys. Rev. B **71**, 045207 (2005).
[35] J. Heyd, G. E. Scuseria, and M. Ernzerhof, J. Chem. Phys. **118**, 8207 (2003).
[36] K. Hummer (unpublished).
[37] J. Camassel, D. Auvergne, H. Mathieu, R. Triboulet, and Y. Marfaing, Solid State Commun. **13**, 63 (1973).
[38] D. Eich, K. Ortner, U. Groh, Z. H. Chen, C. R. Becker, G. Landwehr, R. Fink, and E. Umbach, Phys. Status Solidi (a) **173**, 261 (1999).
[39] X. Dai, T. L. Hughes, X.-L. Qi, Z. Fang, and S.-C. Zhang, Phys. Rev. B **77**, 125319 (2008).
[40] Y. A. Bychkov and E. I. Rashba, J. Phys. C: Solid State Phys. **17**, 6039 (1984).